# Supplementary Information - A scaling law to determine phase morphologies during ion intercalation

Dimitrios Fraggedakis[1],* Neel Nadkarni[1],* Tao Gao[1],* Tingtao Zhou[2], Yirui Zhang[4], Yu Han[1], Ryan M. Stephens[3], Yang Shao-Horn[4,5], and Martin Z. Bazant[1,6†]

[1] *Department of Chemical Engineering, Massachusetts Institute of Technology, Cambridge, MA 02139 USA*
[2] *Department of Physics, Massachusetts Institute of Technology, Cambridge, MA 02139 USA*
[3] *Shell International Exploration & Production Inc., Houston, Texas 77082, USA*
[4] *Department of Mechanical Engineering, Massachusetts Institute of Technology, Cambridge, MA 02139 USA*
[5] *Department of Materials Science and Engineering, Massachusetts Institute of Technology, Cambridge, MA 02139 USA and*
[6] *Department of Mathematics, Massachusetts Institute of Technology, Cambridge, MA 02139 USA*

(Dated: May 22, 2020)

## DERIVATION OF THE SCALING CRITERION

Our theory is independent of the constitutive relations used to describe the diffusion and kinetics processes. While our simulations are based on a specific model, our analysis as well our conclusions are general for any phase-separating system undergoing heterogeneous reactions. For the ease of visualization and without loss of generality we focus our analysis on a 2D domain, fig. 1.

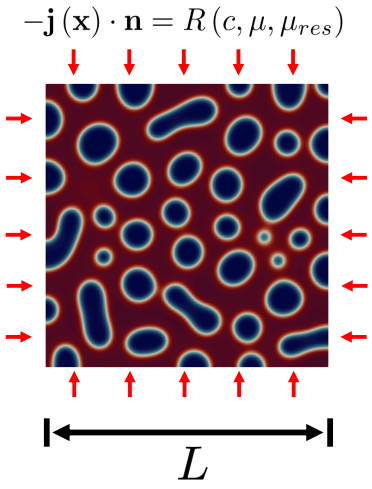


FIG. 1. System of volume $V$ and characteristic length $L$ undergoing insertion kinetics. For demonstration purposes, we show a solution undergoing spinodal decomposition, the timescale of which play a fundamental role on defining if the process is reaction or diffusion limited.

The concentration profile $c$ in a domain of characteristic length $L$ is described by

$$\frac{\partial c}{\partial t} = -\nabla\cdot\mathbf{j} \tag{1}$$

where $\mathbf{j}$ is the diffusive flux defined in terms of the species chemical potential gradient $\mathbf{j} = -M(c)\nabla\mu$, $\nabla$ is the gradient operator and $M(c)$ is the species mobility and depends on the concentration [1].

A heterogeneous reaction of the form

$$C_{res} \leftrightarrows C$$

takes place at the boundary of the domain which is described by the following boundary conditions

$$-\mathbf{n}\cdot\mathbf{j} = R \tag{2}$$

with $R = R(c,\mu,\mu_{res})$ the reaction rate which depends on the species concentration, its chemical potential and the reservoir species chemical potential $\mu_{res}$ [2–7]. In electrochemical systems it is common practice to drive the reaction under galvanostatic conditions [8]. This is equivalent as keeping the total reaction rate $R_t$ across the reactive boundary at a constant value

$$-\int_{\partial A}\mathbf{n}\cdot\mathbf{j}\,dA = \int_{\partial A} R\,dA = R_t \tag{3}$$

The mean concentration of $C$ in the domain shown in fig. 1 is defined as

$$\frac{d\langle c\rangle}{dt} = \frac{1}{V}\int_{\partial A} R\,dA = \frac{R_t}{V} \tag{4}$$

where $V$ (in $\mathrm{m}^3$) is the volume of the system.

Both eqs. 3 and 4 play a central role in our analysis, as we use them to define the scaling relation which quantifies if our system is reaction or diffusion limited. First, we need to transform both of them in a dimensionless form. To do so, as a characteristic reaction rate we choose $k_0/F$, where $k_0$ is in units of $\mathrm{A/m^2}$ and F is the Faraday constant. Additionally, the characteristic scale for the differential area of the reaction integral $dA$ is the total area of the reactive boundaries $A$ (in $\mathrm{m}^2$). The flux $\mathbf{j}$ and the total concentration are scaled with $D_{ch}c_{max}/L$ and $c_{max}$, respectively, where $D_{ch}$ is a characteristic diffusivity (in $\mathrm{m}^2/\mathrm{s}$) and $c_{max}$ is the maximum concentration we can store in the domain. Applying these scales in both eqs. 3 & 4, it results

$$-\int_{\partial A}\mathbf{n}\cdot\widetilde{\mathbf{j}}\,d\widetilde{A} = Da\int_{\partial A}\widetilde{R}\,d\widetilde{A} \tag{5a}$$

* equal contributions
† corresponding author: bazant@mit.edu

$$\int_{\partial A} \widetilde{R}\, d\widetilde{A} = \frac{R_t}{\frac{k_0 L^2}{F}} = \widetilde{R}_t \tag{5b}$$

with $k_0 L^2/F$ being the characteristic overall insertion rate. In equation 5a we define the Damköhler number as $Da = k_0 L/DFc_{max}$, with $L = V/A$. Combining eqs. 5a & 5b we arrive in a relation which connects the diffusive flux at the boundaries of the system with the total imposed insertion rate

$$-\int_{\partial A} \mathbf{n}\cdot\widetilde{\mathbf{j}}\, d\widetilde{A} = Da \times \widetilde{R}_t \tag{6}$$

When the reaction is electrochemical in nature, $\widetilde{R}_t = I$, where $I$ is the dimensionless applied current in the system.

From eq. 6, we understand there is an interplay between the diffusive flux and the insertion kinetics. More specifically, the one that is slower is going to be the rate determining step. In cases where diffusion in the material is large, such that quasi-static equilibrium is achieved, then reactions are controlling the process. On the other hand, where insertion kinetics are very fast compared to the slowest diffusion timescale in the system, then diffusion is the bottleneck. In the case of phase separating materials, the system exhibits more complex phenomena compared to the well-understood diffusion [9]. More specifically, once system is thermodynamically unstable, the mixture will no longer be a solid solution and spinodal decomposition takes place, fig. 1. A well-known phenomenon when a system undergoes phase separation is the coarsening of phases [10]. According to non-equilibrium thermodynamics, the diffusivity of the slowest phase determine the coarsening timescale. Therefore, as the characteristic diffusivity in the $Da$ number, we should choose the diffusivity of the slowest phase, as the slow coarsening dynamics of the slowest phase can lead to a diffusion-limited system.

To conclude our findings, from eq. 6 we known that when $Da \times \widetilde{R}_t > 1$, diffusion-related phenomena cannot keep up with the insertion kinetics, and thus diffusion-limitations are expected to be experienced. On the other hand, for $Da \times \widetilde{R}_t < 1$, once new chemical species enter the domain, diffusion is fast enough to make the system be at quasi-static equilibrium. These simple arguments, which are based on dimensionless analysis between phenomena of different timescales, are validated by full three-dimensional simulations in the main text.

## DETAILS FOR LITHIUM COBALT OXIDE SYSTEM

$Li_xCoO_2$ (LCO) [11] is a layered oxide, widely used in commercial Li-ion batteries [12, 13]. When x $\in [0.5, 1.0]$, $Li_xCoO_2$ belongs to the R$\bar{3}$m space group, and has a hexagonal close-packed structure with rhombohedral symmetry [14, 15]. Between $0.75 < x < 0.94$, LCO undergoes a metal-insulator transition, changing the layered oxide from a perfect to a poor conductor [16]. As revealed by *ab-initio* calculations, Li ions diffuse mostly through tetrahedral site hopping (TSH) [17], and this occurs only along the $xy$ planes, not allowing for intra-layer diffusion. Figs.1(b) and (c) in the main text show a single crystal nanoparticle of $Li_xCoO_2$ undergoing $Li^+$ intercalation under constant current conditions [11]. Li ions are inserted from the sides of the particle, while the top and the bottom sides are impermeable. Another characteristic of our system is the negligible diffusivity along $z$-direction, which is responsible for kinetically-arrested equilibrium states [11].

The homogeneous free energy $g_h$ has the following functional form

$$\begin{aligned} g_h(c) =& \mu^0 c + RT\left[c\log c + (1-c)\log(1-c)\right] \\ &+ c(1-c)\sum_{k=1}^{N}\Omega_k (1-2c)^{k-1} \end{aligned} \tag{7}$$

where $N = 3$ and $\Omega_1 = -159744$ J/mol, $\Omega_2 = -118782$ J/mol, $\Omega_3 = -39032$ J/mol. Additionally, the penalty gradient constant $\kappa = 3.084 \times 10^{-18}$ J/m.

The mobility of Li ions in LCO was fitted to the *ab-initio* calculation found in [18]. The fitted expression is

$$\begin{aligned} M(c) =& \frac{1}{c}\exp\left[\log(10)\left(119.8260c^3\right.\right. \\ &\left.\left. -305.4364c^2 + 245.7523c - 76.2585\right)\right] \end{aligned} \tag{8}$$

The functional form is shown in fig. 2.

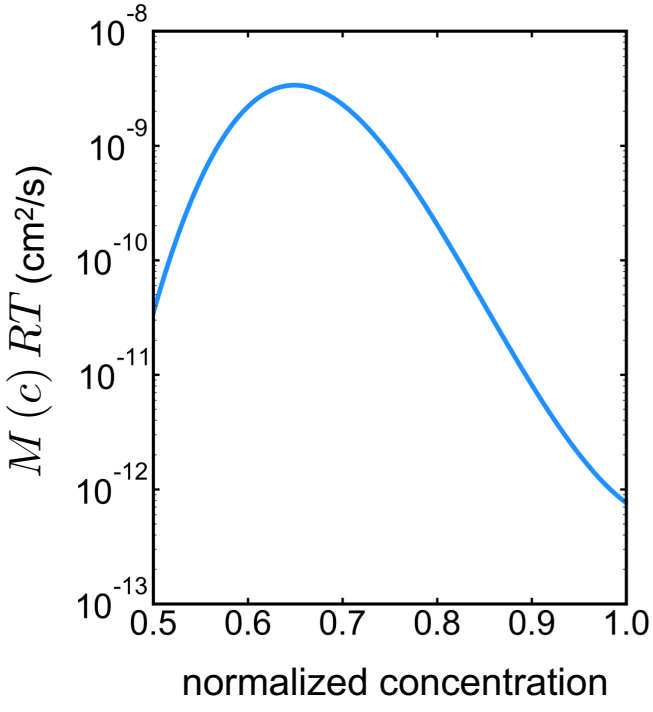


FIG. 2. Mobility $M(c)$ as a function of the fractional concentration $c$.

## IMPLICATIONS ON THE PREDICTION OF THE OVERPOTENTIAL

The spatial dependence of the concentration profile has practical implications on the predicted overpotential. In phase-separating systems, during insertion, we show that the Li-rich phase always forms at a boundary of the particles, Fig.2. Therefore, when the system is modeled using the reduced-dimension model, the shrinking-core structure is going always to be formed, with the Li-rich phase to be located at the reactive boundary. In general, there is a critical concentration value after which the insertion reaction rate decreases monotonically [2, 8, 19], and in the limit of x $\rightarrow$ 1 the reaction shuts down. When ion insertion is driven galvanostatically, by the time the boundary concentration lies inside the spinodal the solution undergoes phase separation [20, 21]. At this moment the value of Li concentration along the boundary of the entire system becomes that of the Li-rich phase (formation of shrinking-core).

When the concentration of the Li-rich phase approaches x $\rightarrow$ 1, the effective resistance of the reaction becomes infinite [3]. Therefore, in order for the system to keep up with the applied current, the overpotential has to increase resulting in the voltage to reach its cut-off limit. In the case where the concentration profile is allowed to depend in three dimensions, the overpotential does not overshoot. The main reason is that Li ions are inserted at the side of the interface that results in smaller overall overpotential [11].

Depending on the value of the applied current, the spike in the overpotential predicted by the shrinking-core model can force the resulting voltage to drop below its cut-off value. This is highly likely to underestimate the final state of (dis)change (SOC/D) of the system. In the case of anode materials, such as graphite, the prediction of larger overpotential values can lead to false predictions about the conditions where Li plating becomes thermodynamically favorable. Thus, it can result in falsified and costly decisions for designing the electrochemical experiments/systems.

## DETAILS ON THE *IN-SITU* OPTICAL MICROSCOPY EXPERIMENT

### Apparatus and experiment

The experiment was done in a custom cell, in which a working electrode/separator/Li counter electrode sandwich was pushed against spacer and washer by a quartz window. The working electrode consists of graphite flake particles loaded onto a stainless-steel mesh. The size of the graphite flakes varies between 354-420 $\mu$m, which is controlled by sieving the commercial graphite flake (Sigma-Aldrich) through a mesh 40 sieve followed by a mesh 45 sieve. The electrolyte is 1M $LiPF_6$-EC-EMC. We use a digital camera to record the graphite electrode during charge/discharge. There are roughly $\sim$ 60 particles loaded, Fig. 3.

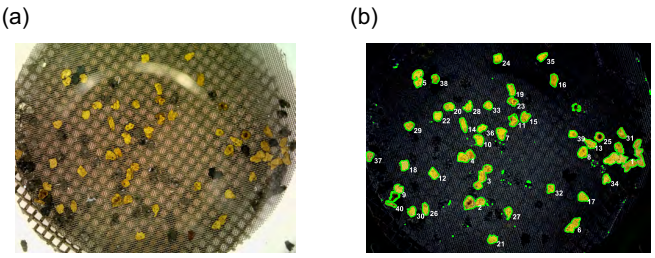


FIG. 3. Image of the experimental device where $Li_xC_6$ particles undergo lithiation. (a) Electrochemical cell where the graphite particles are sitting on the electrode mesh. (b) Image processed particles to identify their shape as well as their color change during lithiation.

### Analysis on core-shell statistics

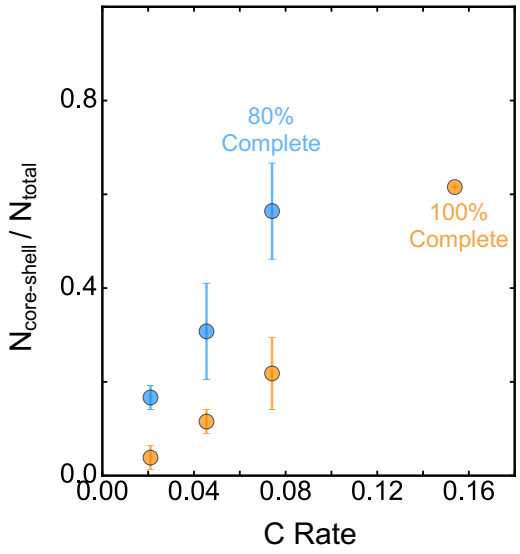


FIG. 4. Statistical analysis on the number of particles that undergo core-shell lithiation, $N_{\text{core-shell}}$, as a function of the applied C Rate. We observe the fraction of the particles that have a shrinking-core behavior to increase linearly with increasing C Rate. Two different measurements at two different overall completion percentage were considered, 80% and 100%, respectively. The completion is defined as the time where the voltage of the cell is equal to 0V vs Li.

## PHASE-SEPARATION PROFILES FOR DIFFERENT DIFFUSION MECHANISMS

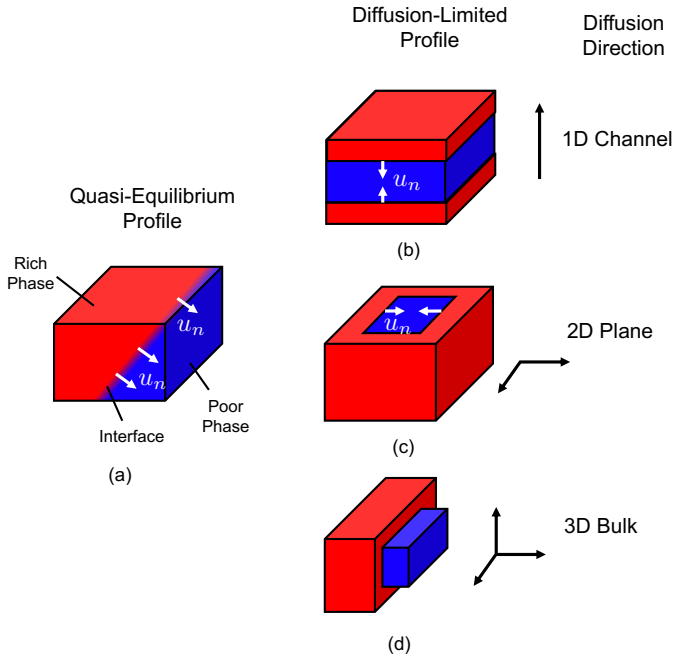


FIG. 5. Demonstration of the concentration profile under reaction and diffusion limitations. Different diffusion mechanisms are illustrated in (b) to (c). (b) species are able to diffuse through 1D channels, e.g. $Li_xFePO_4$ [22]. (c) species can only diffuse *via* an in-plane mechanism, e.g. $Li_xCoO_2$ [17], $Li_xC_6$ [23]. (d) species can diffuse in every direction, e.g. $Li_4Ti_5O_{12}$ [24]. Under diffusion limitations, each diffusion mechanism leads to different concentration as shown in figures (b) to (c).

## LITERATURE DATA FOR THE TRANSITION BETWEEN THE BULK QUASI-EQUILIBRIUM AND DIFFUSION-LIMITED REGIME

To further validate our predictions on the scaling law that classifies the observed phase morphologies, we resort to reported literature data on $Li_xC_6$ (graphite), $Li_xCoO_2$ (LCO) and $Li_xFePO_4$ (LFP). A lot of experimental work has been reported on trying to understand the dynamics of phase separation in LFP and $Li_xC_6$ systems, and how these dynamics affect the performance of Li-ion batteries. In the following table, we report the gathered data from *in-situ* electrochemical and chemical lithiation/delithiation, where direct visualization of phase separation dynamics was performed.

Only one reference for chemical delithiation of LFP is used [25], where the 'C Rate' is approximated as follows: based on the available data, it is estimated that when the surface of the LFP crystal is exposed to the electrolyte, the chemical potential difference between the reactant and product state is equivalent to 1V. Given this is a chemical delithiation process, and neglecting all the electron transfer effects [26], we approximate the resulting current upon exposure with the expression of Butler-Volmer kinetics presented in [2, 6, 21]. Using as exchange current density the one reported in [26], and considering the binodal points of LFP to be at $x \simeq 0.05$ and $x \simeq 0.95$, we find that the value of the 'chemical C Rate' to be C Rate $\simeq 7.49$ $h^{-1}$.

For the construction of the master plot shown in Fig.4b of the main text, we estimate the exchange current density based on literature data. For LCO we consider $i_0 \sim 10^{-3}$ A/m$^2$ [11], for LFP $i_0 \sim 10^{-2}$ A/m$^2$ [27], and for graphite $i_0 \sim 10^{-2}$ A/m$^2$ [28, 29].


[1] S. R. De Groot and P. Mazur, *Non-equilibrium thermodynamics* (Courier Corporation, 2013).
[2] M. Z. Bazant, Accounts of Chemical Research **46**, 1144 (2013).
[3] M. Z. Bazant, Faraday Discussions (2017), 10.1039/C7FD00037E.
[4] D. Fraggedakis, R. B. Smith, M. McEldrew, Y. Krishnan, W. Chueh, P. Bai, and M. Z. Bazant, "Theory of mixed ion-electron transfer kinetics in concentrated solutions and solids," (2018).
[5] D. Fraggedakis and M. Z. Bazant, "Tuning of electrochemical interfaces by electron transfer (et) reactions," (2019).
[6] N. Nadkarni, E. Rejovitsky, D. Fraggedakis, C. V. Di Leo, R. B. Smith, P. Bai, and M. Z. Bazant, Physical Review Materials **2**, 085406 (2018).
[7] Y. Li, H. Chen, K. Lim, H. D. Deng, J. Lim, D. Fraggedakis, P. M. Attia, S. C. Lee, N. Jin, J. Moškon, Z. Guan, W. E. Gent, J. Hong, Y. S. Yu, M. Gaberšček, M. S. Islam, M. Z. Bazant, and W. C. Chueh, Nature Materials **17**, 915 (2018).
[8] J. Newman and K. E. Thomas-Alyea, *Electrochemical Systems*, 3rd ed. (John Wiley and Sons, Hoboken, New Jersey, 2004).
[9] T. F. Fuller, M. Doyle, and J. Newman, Journal of The Electrochemical Society **141**, 1 (1994).
[10] A. Bray, Philosophical Transactions of the Royal Society of London. Series A: Mathematical, Physical and Engineering Sciences **361**, 781 (2003).
[11] N. Nadkarni, T. Zhou, D. Fraggedakis, T. Gao, and M. Z. Bazant, Advanced Functional Materials (2019).
[12] K. Mizushima, P. C. Jones, P. J. Wiseman, and J. B. Goodenough, Solid State Ionics **3-4**, 171 (1981).
[13] N. Nitta, F. Wu, J. T. Lee, and G. Yushin, Materials Today **18**, 252 (2015).
[14] A. Van der Ven, M. K. Aydinol, and G. Ceder, Journal of The Electrochemical Society **145**, 2149 (1998).
[15] Y. Shao-Horn, L. Croguennec, C. Delmas, E. C. Nelson, and M. A. O'Keefe, Nature materials **2**, 464 (2003).
[16] C. A. Marianetti, G. Kotliar, and G. Ceder, Nature materials **3**, 627 (2004).
[17] A. Van der Ven and G. Ceder, Electrochemical and Solid-State Letters **3**, 301 (2000).
[18] A. Van der Ven and G. Ceder, Electrochemical and Solid-State Letters **3**, 301 (2000).
[19] V. Srinivasan and J. Newman, Electrochemical and Solid-State Letters **9**, A110 (2006).
[20] P. Bai, D. A. Cogswell, and M. Z. Bazant, Nano letters **11**, 4890 (2011).
[21] D. A. Cogswell and M. Z. Bazant, ACS nano **6**, 2215 (2012).
[22] R. Malik, D. Burch, M. Bazant, and G. Ceder, Nano Letters **10**, 4123 (2010).
[23] K. Persson, Y. Hinuma, Y. S. Meng, A. Van der Ven, and G. Ceder, Physical Review B **82** (2010), 10.1103/PhysRevB.82.125416.
[24] B. Ziebarth, M. Klinsmann, T. Eckl, and C. Elsässer, Physical Review B - Condensed Matter and Materials Physics **89**, 1 (2014).
[25] K. Weichert, W. Sigle, P. A. van Aken, J. Jamnik, C. Zhu, R. Amin, T. Acarturk, U. Starke, and J. Maier, Journal of the American Chemical Society **134**, 2988 (2012).
[26] P. Bai and M. Z. Bazant, Nature Communications **5** (2014), 10.1038/ncomms4585.
[27] J. Lim, Y. Li, D. H. Alsem, H. So, S. C. Lee, P. Bai, D. A. Cogswell, X. Liu, N. Jin, Y.-s. Yu, N. J. Salmon, D. A. Shapiro, M. Z. Bazant, T. Tyliszczak, and W. C. Chueh, Science **353**, 566 (2016).
[28] Y. Guo, R. B. Smith, Z. Yu, D. K. Efetov, J. Wang, P. Kim, M. Z. Bazant, and L. E. Brus, The Journal of Physical Chemistry Letters **7**, 2151 (2016).
[29] T. Gao, Y. Han, D. Fraggedakis, T. Zhou, S. Das, C.-N. Yeh, S. Xu, W. C. Chueh, J. Li, and M. Z. Bazant, "Interplay of lithium intercalation and plating in single graphite particle," (2020).
[30] X. Zhang, M. Van Hulzen, D. P. Singh, A. Brownrigg, J. P. Wright, N. H. Van Dijk, and M. Wagemaker, Nature communications **6**, 8333 (2015).

| Material and Ref. | $V/A$ | Estimated C Rate(s) ($h^{-1}$) | Morphology |
|---|---|---|---|
| LFP [27] | 150 nm | 0.2, 0.6, 2.0 | Intercalation Wave |
| LFP [30] | 36 nm | 0.5, 2.0 | Intercalation Wave |
| LFP [31] | 25 $\mu$m | 0.2 | Intercalation Wave |
| LFP [32] | 500 nm | 0.1, 0.2 | Intercalation Wave |
| LFP [33] | 20 nm, 150 nm, 250 nm | 0.1 | Intercalation Wave |
| Chemical LFP [25] | 1.3 mm | $\sim$7.49 | Shrinking Core |
| Graphite [34] | 4 $\mu$m | 0.2, 0.5 | Intercalation Wave |
| Graphite [28] | 50 $\mu$m | 3 | Shrinking Core |
| Graphite [29] | 1 mm | 0.1 | Shrinking Core |
| LCO [35] | 10 $\mu$m | 0.1 | Intercalation Wave |
| LCO [35] | 10 $\mu$m | 1 | Intercalation Wave/Shrinking Core |
| LCO [35] | 10 $\mu$m | 10 | Shrinking Core |

TABLE I. Literature data on the classification of phase separation dynamics during (de)lithiation. Results for LFP, Graphite and LCO are reported.


[31] L. Hong, L. Li, Y.-K. Chen-Wiegart, J. Wang, K. Xiang, L. Gan, W. Li, F. Meng, F. Wang, J. Wang, Y.-M. Chiang, S. Jin, and M. Tang, Nature Communications **8**, 1194 (2017).

[32] J. Wang, Y.-c. K. Chen-Wiegart, and J. Wang, Nature communications **5**, 1 (2014).

[33] Y.-S. Yu, C. Kim, D. A. Shapiro, M. Farmand, D. Qian, T. Tyliszczak, A. D. Kilcoyne, R. Celestre, S. Marchesini, J. Joseph, *et al.*, Nano letters **15**, 4282 (2015).

[34] K. E. Thomas-Alyea, C. Jung, R. B. Smith, and M. Z. Bazant, Journal of The Electrochemical Society **164**, E3063 (2017).

[35] Y. Xu, E. Hu, K. Zhang, X. Wang, V. Borzenets, Z. Sun, P. Pianetta, X. Yu, Y. Liu, X.-Q. Yang, *et al.*, ACS Energy Letters **2**, 1240 (2017).